Radial evolution of the electron distribution functions in the fast solar wind between 0.3 and 1.5 AU

M. Maksimovic, I. Zouganelis, Jean-Yves Chaufray, K. Issautier, E. E. Scime, J. E. Littleton, E. Marsch, D. J. Mccomas, C. Salem, R. P. Lin, et al.

▶ **To cite this version:**

M. Maksimovic, I. Zouganelis, Jean-Yves Chaufray, K. Issautier, E. E. Scime, et al.. Radial evolution of the electron distribution functions in the fast solar wind between 0.3 and 1.5 AU. Journal of Geophysical Research Space Physics, 2005, 110 (A9), pp.A09104. ⟨10.1029/2005JA011119⟩. ⟨insu-02155267⟩

HAL Id: insu-02155267

https://insu.hal.science/insu-02155267v1

Submitted on 17 Jun 2019

HAL is a multi-disciplinary open access archive for the deposit and dissemination of scientific research documents, whether they are published or not. The documents may come from teaching and research institutions in France or abroad, or from public or private research centers.

L'archive ouverte pluridisciplinaire **HAL**, est destinée au dépôt et à la diffusion de documents scientifiques de niveau recherche, publiés ou non, émanant des établissements d'enseignement et de recherche français ou étrangers, des laboratoires publics ou privés.

HAL Authorization

Radial evolution of the electron distribution functions in the fast solar wind between 0.3 and 1.5 AU

M. Maksimovic,[1] I. Zouganelis,[1] J.-Y. Chaufray,[1,2] K. Issautier,[1] E. E. Scime,[3] J. E. Littleton,[3] E. Marsch,[4] D. J. McComas,[5] C. Salem,[6] R. P. Lin,[6,7] and H. Elliott[5]

Received 3 March 2005; revised 27 April 2005; accepted 11 May 2005; published 21 September 2005.

[1] Observed electron distribution functions of the solar wind permanently exhibit three different components: a thermal core and a suprathermal halo, which are always present at all pitch angles, and a sharply magnetic field aligned "strahl" which is usually anti-sunward moving. Whereas Coulomb collisions can explain the relative isotropy of the core population, the origin of the halo population, and more specifically the origin of its sunward directed part, remains unknown. In this study we present the radial evolution of the electron velocity distribution functions in the fast solar wind between 0.3 and 1.5 AU. For this purpose we combine data measured separately by the Helios, Wind, and Ulysses spacecraft. We compute average distributions over distance and normalize them to 1 AU to remove the effects of the solar wind expansion. Then we model separately the core, halo, and strahl components to compute their relative number density or fraction of the total electron density. We observe that, while the core fractional density remains roughly constant with radial distance, the halo and strahl fractional densities vary in an opposite way. The relative number of halo electrons is increasing, while the relative number of strahl electrons is decreasing with distance. Therefore we provide, for the first time, strong evidences for a scenario that is commonly assumed: the heliospheric electron halo population consists partly of electrons that have been scattered out of the strahl.

Citation: Maksimovic, M., et al. (2005), Radial evolution of the electron distribution functions in the fast solar wind between 0.3 and 1.5 AU, *J. Geophys. Res.*, *110*, A09104, doi:10.1029/2005JA011119.

1. Introduction

[2] Observed electron velocity distribution functions (eVDFs) of the solar wind permanently exhibit three different components: a thermal core and a suprathermal halo, which are always present at all pitch angles, and a sharply magnetic field aligned "strahl" which is usually anti-sunward moving [*Montgomery et al.*, 1968; *Feldman et al.*, 1975; *Rosenbauer et al.*, 1977; *Pilipp et al.*, 1987]. At 1 AU, the core has a typical temperature of 10^5 K and represents about 95% of the total electron number density. The halo population has a typical temperature of 7×10^5 K and represents together with the strahl the remaining portion of the total electron number density.

[3] In the ecliptic plane from 1 to 5 AU, the halo to core density ratio is observed to remain constant with heliocentric distance [*McComas et al.*, 1992] at a value of $\approx$4%, and the strahl is predominantly observed in high-speed solar winds [*Rosenbauer et al.*, 1977; *Pilipp et al.*, 1987]. Out of the ecliptic, in the fast wind, the strahl angular width is observed to broaden with increasing heliospheric distance [*Hammond et al.*, 1996]. This result, somehow not enough recognized in the literature, is in contradiction with the largely disseminated idea that the strahl electrons are remnants of the hot coronal electrons which escape into the interplanetary medium without suffering collisions and therefore conserve their magnetic moments.

[4] What is the origin of the non-Maxwellian eVDFs observed in the solar wind? Are such distributions already present in the solar corona or are they only a consequence of the solar wind transport in the interplanetary medium? There is an increasing amount of both theoretical [*Vinas et al.*, 2000; *Leubner*, 2002; *Dorelli and Scudder*, 2003; *Landi and Pantellini*, 2001; *Vocks and Mann*, 2003] and observational [*Ko et al.*, 1998; *Pinfield et al.*, 1999; *Esser and Edgar*, 2000; *Chiuderi and Chiuderi Drago*, 2004] evidences that tends to show that nonthermal VDFs can develop and exist in the high corona and even in the

[1]LESIA and CNRS, Observatoire de Paris-Meudon, Meudon, France.
[2]Now at Service d'Aéronomie du CNRS, Verrières Le Buisson, France.
[3]Department of Physics, West Virginia University, Morgantown, West Virginia, USA.
[4]Max-Planck-Institut für Sonnensystemforschung, Katlenburg-Lindau, Germany.
[5]Space Science and Engineering Division, Southwest Research Institute, San Antonio, Texas, USA.
[6]Space Sciences Laboratory, University of California, Berkeley, California, USA.
[7]Also at Physics Department, University of California, Berkeley, California, USA.

Copyright 2005 by the American Geophysical Union.
0148-0227/05/2005JA011119

transition region. This is because, in a plasma, the particle mean free paths increase rapidly with speed ($\propto v^4$), so that high-energy tails can develop for Knudsen numbers as low as 10^{-3} [*Shoub*, 1983], that is, even in a semicollisional plasma. Even more, high-energy tails can be expected to be found in the weakly collisional corona and solar wind acceleration region. However, until now, there have not been any conclusive observations that have settled the question of the shape of the eVDFS in the corona.

[5] With purely collisional fluid models, the question of the origin of the electron distributions cannot be answered since these models intrinsically cannot handle suprathermal tails for the eVDFs. If the collisions are completely neglected then the exospheric approach may be adopted [*Maksimovic et al.*, 1997a; *Zouganelis et al.*, 2004]. In this case, the shape of the eVDFs can be obtained from simple Liouville mapping and depends strongly on the radial evolution of the interplanetary ambipolar potential $\Phi_E(r)$. Basically, the shape of the core component remains unchanged with distance. The halo is truncated along the radial direction and has no electrons with absolute velocities in the sunward direction above the local escape velocity, which for the electron is $\approx\sqrt{2e\phi_E(r)/m_e}$ [*Maksimovic et al.*, 2001]. At 1 AU, the escape energy is about 100 eV. Since the halo is observed to extend in the sunward direction to energies well beyond this value, the simple exospheric approach alone cannot explain the shape of the observed eVDFs. By way of improvement, *Lie-Svendsen et al.* [1997] and *Pierrard et al.* [1999, 2001] have added Coulomb collisions to the simple exospheric solar wind model. These authors have solved the time-stationary Fokker-Planck equations for test particles colliding with a background plasma. They have used a specific operator for Coulomb collisions and have included the electric ambipolar field as an external force. Despite the authors conclusions, the *Lie-Svendsen et al.* [1997] model does not explain the observed solar wind eVDFs. In this model, only the strahl component is produced by magnetic moment conservation. The halo component in the sunward direction is missing [see *Lie-Svendsen et al.*, 1997, Figure 5]. The *Pierrard et al.* [1999] model does not either explain the observed distributions. In this latter model the halo is present at all radial distances, only if its sunward part is imposed as a boundary condition at 1 AU. In this case the solutions of the time-stationary Fokker-Planck equation yield VDFs which are also nonthermal in the corona.

[6] Processes invoking scattering of strahl electrons by shocks or corotating interaction regions (CIRs) have been invoked to explain the existence of the halo component [see, e.g., *Gosling et al.*, 2001]. However, such mechanisms, even if they could play a role near the ecliptic plane at Solar minimum, where most of the shocks and CIRs are observed, probably cannot explain the eVDFs in the fast solar wind at high latitudes.

[7] In the present article we study the radial evolution of the eVDFs in the fast solar wind between 0.3 and 1.5 AU. We combine data measured separately by the Helios, Wind and Ulysses spacecraft. We model separately the core, halo and strahl components and deduce their individual radial behaviors. In section 2 we present the data we used and discuss the specific analysis we have developed to normalize the distributions and remove the effects of the solar wind expansion. In section 3 we present the results of our analysis and finally give some conclusions in section 4.

Table 1. Time Intervals Used for the Study[a]

Spacecraft	Time Periods,[b] DOY	Heliocentric Distance Coverage, AU
	1976	
HELIOS 1	68–71	
	123–126	0.3–0.41
	305–308	
HELIOS 2	91–94	
	120–123	0.475–0.53
	289–293	
	298–301	0.7–0.75
	1995	
WIND	06, 21; 0000–1600 UT	1
Ulysses	12–37	1.35–1.5
	89–132	

[a]For Wind and Ulysses the time intervals correspond to minima of solar activity. For Ulysses, the selected periods correspond to portions of the first south and north polar passes.
[b]DOY, days of year.

2. The Data Analysis

[8] The purpose of the present work is to study the radial evolution of the electron distribution functions over a wide heliocentric distance range. There is no single space mission that has explored the inner heliosphere in the range 0.3 to 1.5 AU. Therefore we combine solar wind electron data measured separately by the Helios, Wind and Ulysses spacecraft during time intervals corresponding to minima of solar activity. The time intervals used for the study are reported in Table 1. For Ulysses, the selected periods correspond to portions of the first south and north polar passes. As we wish to restrict this study to the steady state fast solar wind, we select, for the three probes, only data for which the solar wind bulk speed is larger than 650 km/s. This way, we constructed a data set that we assume to be representative of the steady state, time-stationary, spherically symmetric, fast solar wind, observed in the range between 0.3 and 1.5 AU. To check this important assumption, we display in Figure 1 the normalized solar wind flux N_iVr^2 as a function of the heliospheric distance r, with N_i being the total, proton plus helium, ion number density. In this figure, the data are divided into radial bins of 0.1 AU in width. In each of the radial bins we compute the median values of the flux distributions and the corresponding standard deviation around these medians. The median values of the normalized flux are represented by three different symbols corresponding to the three spacecraft, and the standard deviations are represented by error bars. As one can see, the assumption of a steady state, time-stationary, spherically symmetric solar wind flow is well verified. The normalized flux is relatively constant over the whole radial range. We can now study the radial evolution of the electron velocity distribution functions as measured by the electron instruments aboard Helios, Wind and Ulysses.

[9] On the two Helios probes, the solar wind electrons were observed with nearly identical electron analyzers described by *Schwenn et al.* [1975], *Rosenbauer et al.* [1977] or *Pilipp et al.* [1987]. Basically these instruments

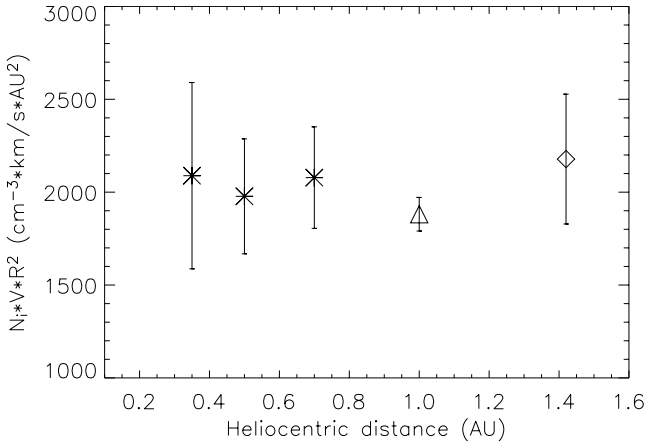

Figure 1. Normalized solar wind flux $N_i V r^2$ as a function of the heliospheric distance r, with N_i being the total, proton plus helium, ion number density. The median values of the normalized flux are represented by three different symbols corresponding to the three spacecraft, and the standard deviations are represented by error bars.

recorded 2-D distribution functions. Their fields of view were perpendicular to the spin axis, i.e., along the ecliptic plane and were narrow in the azimuthal direction (30° and 13° for respectively Helios 1 and 2). The electrons were analyzed with respect to their energies in 32 energy channels between 0.004 eV and 1658 eV.

[10] On the Wind spacecraft, the electrons distributions are measured with the 3-D Plasma experiment [*Lin et al.*, 1995]. This instrument measures three-dimensional electron velocity distributions in 88 angular bins, each with roughly 22° × 22° resolution. In this study, we use data in the low energy range from a few eV to 1100 eV.

[11] On the Ulysses spacecraft, the electron distributions are obtained with the solar wind plasma instrument [*Bame et al.*, 1992]. This instrument measures three-dimensional electron velocity distributions. Electrons with central energies in the range 0.86 eV to 814 eV are detected in many directions which cover the unit sphere comprehensively.

[12] To retrieve the correct solar wind electron distribution functions from the measurements, several corrections need to be done. One has first to distinguish between spacecraft photoelectrons and solar wind electrons. This is performed by removing the data corresponding to energy channels lower than a given threshold energy. The choice of this energy depends on the different energy channel distributions obtained with the three experiments. Then the distributions have to be corrected for spacecraft charging effects due to the emission of photoelectrons as well as with respect to currents from solar wind electrons and protons. Several techniques can be used to determine the spacecraft electric potential. Here we have used those described by *Pilipp et al.* [1987], *Scime et al.* [1994] and *Salem et al.* [2001], respectively for the Helios, Ulysses and Wind instruments. Finally a background level has also to be removed from all the individual distributions. This background is the phase space density corresponding to a one-count-level detection. This background noise is especially important for the Ulysses measurements at large heliocentric distance where the electron fluxes are particularly low.

[13] Once the above corrections are done, the individual electron distributions are defined in a velocity frame with components parallel and perpendicular to the ambient magnetic field and centered on the solar wind proton bulk speed. For Helios, as the instrument measures only 2-D distributions, we select only those data for which the magnetic field vector is close to the ecliptic plane, that is when $B_z/|B| < 0.2$. For all the observed distributions we have also normalized the direction of the electron strahl. As we said in the introduction, the electron strahl is a sharply magnetic-field-aligned component, which is mainly anti-sunward moving in the undisturbed solar wind plasma, i.e., in regions which do not correspond to a specific configuration of the interplanetary magnetic field **B**, such as prevailing in magnetic clouds or other flux ropes. As they move anti-sunward, the strahl electrons can be directed along both +**B** or −**B**, depending on the orientation of the interplanetary magnetic field. For instance on Ulysses, the strahl is mainly directed along −**B** during the south polar pass in 1995 and along +**B** during the successive north polar pass. We therefore turn around the parallel direction of the electron speeds, when needed, in order to have always the strahl electrons directed along +**B**. We also remove all the distributions for which the strahl electrons move sunward. This represents about 2% of our total data set.

[14] We then define radial distance bins r_i, which correspond to the respective heliocentric distance ranges covered by the three spacecraft. There are five radial distance bins, which are given in the last column of Table 1. For each of these radial bins, we compute "average eVDFs" by using the following procedure. We first define velocity bins v_i with width δv_i and pitch angle bins θ_i with widths $\delta\theta_i$, and we compute median values $f^*(v_i, \theta_i)$ of all the phase-space densities $f[v_i - \delta v_i < (v_\parallel^2 + v_\perp^2)^{1/2} < v_i + \delta v_i,\ \theta_i - \delta\theta_i < \theta < \theta_i + \delta\theta_i]$, with $v_\parallel = v \sin\theta$ and $v_\perp = v \cos\theta$. The choice of the θ_i bins corresponds to the angular coverage of the electron instrument on Helios 1. This coverage is represented in Figure 2. Eight angular sectors θ_i, with widths $\delta\theta_i = 15°$, are spaced 45° apart.

[15] Our procedure is equivalent to computing, in each of the r_i bins, four median cuts f^*_5, f^*_{26}, f^*_{37} and f^*_8 corresponding to the angular coverage of Figure 2. By construction, f^*_5 and f^*_{37} are, respectively, the perpendicular $f_\perp(v) = f(v_\parallel = 0, v_\perp)$ and parallel $f_\parallel(v) = f(v_\parallel, v_\perp = 0)$ cuts of the average VDFs.

[16] In Figures 3a and 3b, we display, respectively, the perpendicular f^*_5 and parallel f^*_{37} cuts of the averaged distributions. These latter are represented by five different colors corresponding to the five r_i bins (black, red and blue for Helios; green for Wind; and magenta for Ulysses). As one can see, the flux as well as the thermal width of the VDFs decrease as the heliocentric distance increases. This is due to the decreasing of the solar wind electron density and temperature.

3. Results

3.1. Radial Evolution of Average Electron Distributions

[17] In order to remove from the radial variations of the VDFs those parts which are due to spherical expansion of the solar wind, we compute normalized distributions. As a

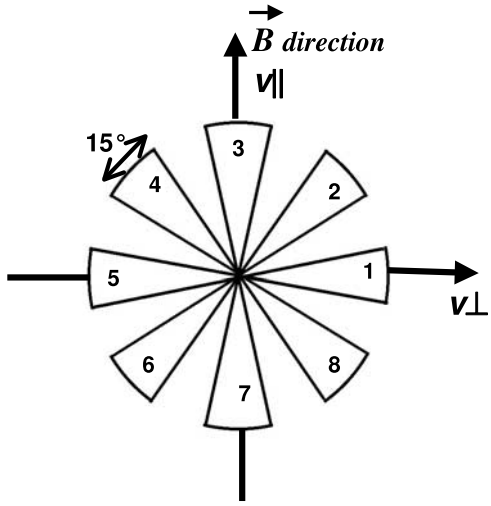

Figure 2. Angular coverage of the electron instrument on Helios 1: eight angular sectors θ_i, with widths $\delta\theta_i = 15°$, are spaced 45° apart from one another. This coverage is used to compute the "average electron velocity distribution functions" (see the text for more details).

first step, we fit the VDFs by a model function. Several models have been used in the past to fit the eVDFs in the solar wind. The classic model is the sum of two bi-Maxwellians [*Feldman et al.*, 1975], one for the core population and one for the halo. Other models have been used, which take into account the fact that the flux at high velocities varies more like a power law rather than a Maxwellian. For instance *Maksimovic et al.* [1997b] modeled Ulysses eVDFs as generalized Lorentzians or kappa functions. After a careful analysis of the data, we use as the best fit the sum of a bi-Maxwellian for the core population plus a bi-kappa for the halo, $f_{mod}(v_\parallel, v_\perp) = f_c(v_\parallel, v_\perp) + f_h(v_\parallel, v_\perp)$. The core $f_c(v_\parallel, v_\perp)$ is defined as:

$$f_c(v_\parallel, v_\perp) = \frac{n_c}{\pi^{3/2}} \frac{1}{V_{\parallel c} V_{\perp c}^2} \exp\left[-\left(\frac{v_\parallel}{V_{\parallel c}}\right)^2 - \left(\frac{v_\perp}{V_{\perp c}}\right)^2 \right]$$

$$V_{\parallel,\perp c} = \sqrt{\frac{2k_B T_{\parallel,\perp c}}{m_e}},$$

where n_c, $T_{\parallel c}$ and $T_{\perp c}$ are, respectively, the core electron density and parallel and perpendicular temperatures. $f_h(v_\parallel, v_\perp)$ is defined by a bi-kappa function:

$$f_h(v_\parallel, v_\perp) = A_\kappa \left(1 + \frac{v_\parallel^2}{\kappa V_{\parallel h}^2} + \frac{v_\perp^2}{\kappa V_{\perp h}^2} \right)^{-\kappa}$$

$$A_\kappa = \frac{n_h}{\pi^{3/2}} \frac{\Gamma(\kappa)}{\kappa^{3/2}\Gamma(\kappa - 3/2)} \frac{1}{V_{\parallel h} V_{\perp h}^2}$$

$$V_{\parallel,\perp h} = \left(\frac{2\kappa - 5}{\kappa} \frac{k_B T_{\parallel,\perp h}}{me} \right)^{1/2},$$

with n_h, $T_{\parallel h}$ and $T_{\perp h}$ being, respectively, the halo electron density and parallel and perpendicular temperatures. The kappa distribution decreases with the speed v as a power law, $f \propto v^{-2\kappa}$. In the limit $\kappa \to \infty$, it reduces to a Maxwellian distribution.

[18] To fit the observed electron distributions, we use a classical χ^2 minimization scheme. At this point, an important point has to be noted concerning our fitting procedure. Our goal is to study the radial variations of the three solar wind populations (core, halo and strahl) separately. Therefore we have to model each of them independently of each other when fitting the observed VDFs. As the model function f_{mod} takes into account only the core and the halo, we have to exclude from the data the angular bins containing the strahl electrons. It is reasonable to assume that the angular extension of the strahl along +**B** never exceeds 150° [*Hammond et al.*, 1996]. Thus we remove from the observed VDFs the data contained in the angular bins 2, 3 and 4 in Figure 2. This implies using the data corresponding to f^*_{15}, $f^*_{26}(v_\parallel < 0)$, $f^*_{37}(v_\parallel < 0)$ and $f^*_{48}(v_\parallel < 0)$. The fitting procedure we apply is described in Appendix A and the reader should refer to it for more details.

[19] The results of the fitting procedures are displayed in Figures 3c, 3d, and 4a–4d. In Figures 3c and 3d, we have overplotted on the observed VDFs, respectively the perpendicular and parallel cuts of the model functions. It can be seen on these figures that the model function f_{mod} provides a good fit to the observed VDFs at all radial distances. The strahl electrons appear also clearly in Figure 3d as an excess in flux compared to the model function for $v_\parallel > 0$. Figure 4a shows for the five r_i bins the total electron number density (from the fitted f_{mod} model) $n_c + n_h$ (squares), the halo density n_h (diamonds), and the median values of the observed ion density $n_{ion} = n_p + 2n_\alpha$ binned over the r_i bins (stars). The error bars on the electron densities are of the order of the symbol size. These error bars will appear more clearly in Figure 7, where we display the relative number densities. We are quite confident in the obtained value of the electron density $n_c + n_h$, since it follows very well the radial evolution of the observed ion density, which itself varies as $r^{-2.2\pm0.1}$. Figure 4b shows the core and halo electron temperatures $T_c = (2T_{\perp c} + T_{\parallel c})/3$ and $T_h = (2T_{\perp h} + T_{\parallel h})/3$, resulting from the fitting of f_{mod}. The errors bars on the electron temperatures are indicated by the vertical lines. The core electron temperature varies as $r^{-0.65\pm0.18}$. This is close to the gradients reported by *Issautier et al.* [1998] or *Maksimovic et al.* [2000] for the fast, high-latitude, solar wind measured by Ulysses. The halo electron temperature is found to vary as $r^{-0.57\pm0.5}$. This gradient is found to be steeper than those usually reported in the literature for the halo component [see *Maksimovic et al.*, 2000, Table 1]. Firstly, this could be due to the fact that we use a bi-kappa function to fit the halo component while, up to now, a bi-Maxwellian has been used in the literature. Secondly, there is a large uncertainty in the power-law index measuring the T_h gradient in Figure 4b. This large uncertainty correspond probably to the visible change in T_h between the radial bins 4 (1 AU) and 5 (1.35 to 1.5 AU). Nevertheless, we cannot exclude from the current analysis and the uncertainty on the T_h gradient that the halo electrons behave rather like an isothermal fluid, as it is usually reported in the literature. In Figure 4c the total electron temperature defined as $(n_c T_c + n_h T_h)/(n_c + n_h)$ is displayed.

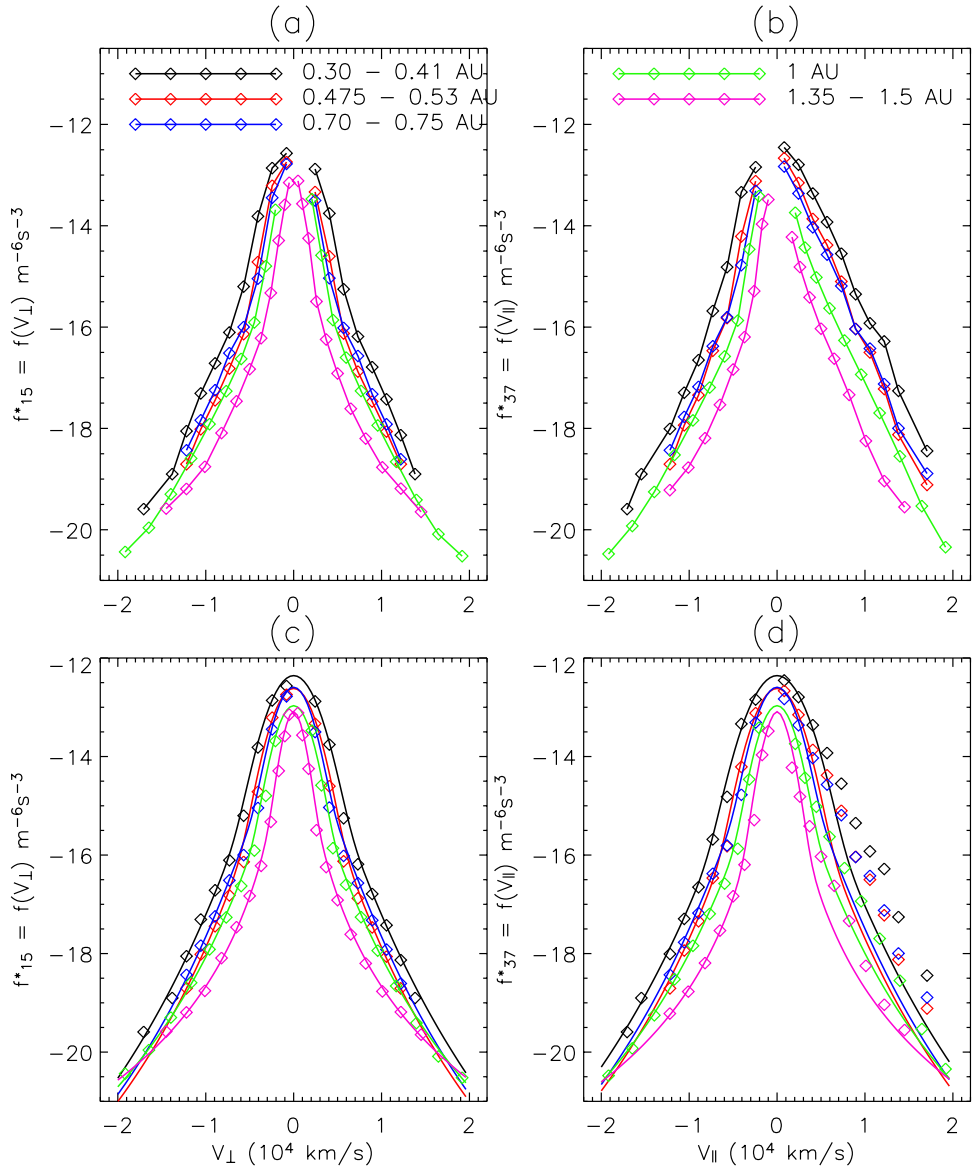

Figure 3. In the top panels the (a) perpendicular f^*_{15} and (b) parallel f^*_{37} cuts of the averaged electron distributions are displayed. The different colors correspond to the five r_i bins (black, red, and blue for Helios; green for Wind; and magenta for Ulysses). In the bottom panels the (c) perpendicular and (d) parallel cuts of the model functions are overplotted on the observed distributions.

It's radial gradient is found to be well represented by the power law $r^{-0.59\pm0.32}$. Finally, the model parameter κ, as obtained from fits to the halo component is displayed on Figure 4d. The errors bars on κ are of the order of the symbol size. An important result can be seen in this figure: κ decreases with the radial distance. This means that in the fast solar wind, the nonthermal tails of the electron VDFs are increasing with radial distance. This is in accordance with the results reported by *Maksimovic et al.* [2000]. Actually for the Helios radial range, the value of the kappa is around 6–7, which is not very far from a Maxwellian. This result can explain the fact that a sum of two bi-Maxwellians was used up to now in the literature. As the radial distance increases, at 1 AU and further, the parameter κ decreases, and it clearly appears that a better model for the observed VDFs is the sum of a Maxwellian plus a kappa function. This is especially the case for the Ulysses observations (P. Riley, private communication, 1998).

3.2. Radial Variation of the Relative Number of Core, Halo, and Strahl Electrons

[20] In addition to the radial behavior of the parameter κ in the f_{mod} function, there is another way of showing that the suprathermal character of the observed VDFs increases with heliocentric distance. The way consists in overplotting all the five radial bins distributions after having normalized them. After having modeled the VDFs, it is possible to remove the radial trends, due to the solar wind spherical symmetric expansion, of both the temper-

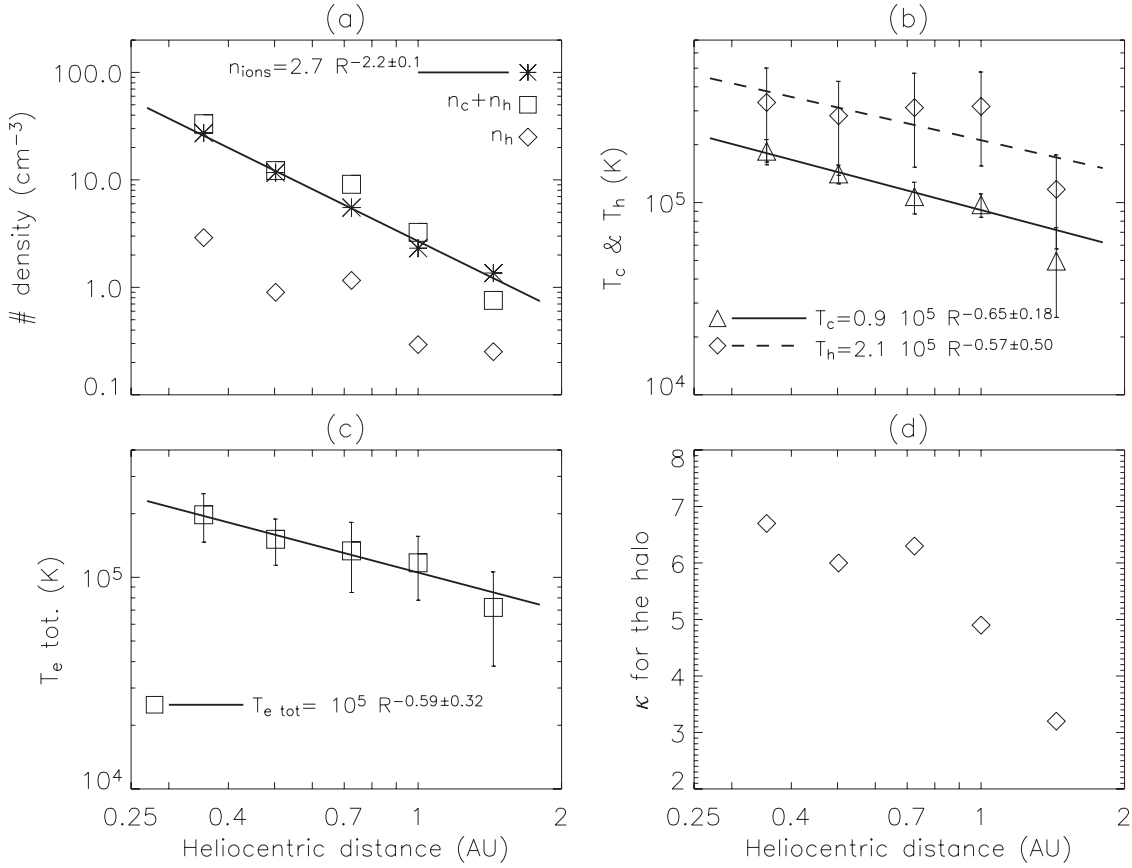

Figure 4. Radial evolution of electron parameters deduced from the fitting of the f_{mod} model. (a) Total electron number density $n_c + n_h$ (squares), the halo density n_h (diamonds), and the median values of the observed ion density $n_{ion} = n_p + 2n_\alpha$ binned over the r_i bins (stars). The error bars on the electron densities are of the order of the symbol size. (b) Core and halo electron temperatures $T_c = (2T_{\perp c} + T_{\|c})/3$ and $T_h = (2T_{\perp h} + T_{\|h})/3$ are displayed. (c) Total electron temperature defined as $T_{etot} = (n_cT_c + n_hT_h)/(n_c + n_h)$ is displayed. (d) Model parameter κ, as obtained from fits to the halo component, is displayed.

ature and particle flux, by plotting $f/f_{mod}(0)$ as a function of $v_\perp/V_c$, where:

$$f_{mod}(0) = \frac{n_c}{\pi^{3/2}} \frac{1}{V_{\|c} V_{\perp c}^2} + A_\kappa$$

and

$$V_c = \sqrt{\frac{2k}{m_e} \frac{2T_{\perp c} + T_{\|c}}{3}}$$

[21] This is what we have done in Figure 5. As we can see, the normalized core component remains unchanged at all radial distances. Obviously, the importance of the normalized halo component is increasing with radial distance. This result can also be understood as being the counterpart to the different radial gradients for T_h and T_c, the latter one being steeper. However, Figure 5 indicates, as a matter of fact, that the relative number of halo electrons, compared to the one of the core, increases with radial distance.

[22] What about the strahl component? What is the radial evolution of it's relative number of electrons? In order to answer this question, we have now to remove the core and halo electrons from the observed distributions, in order to

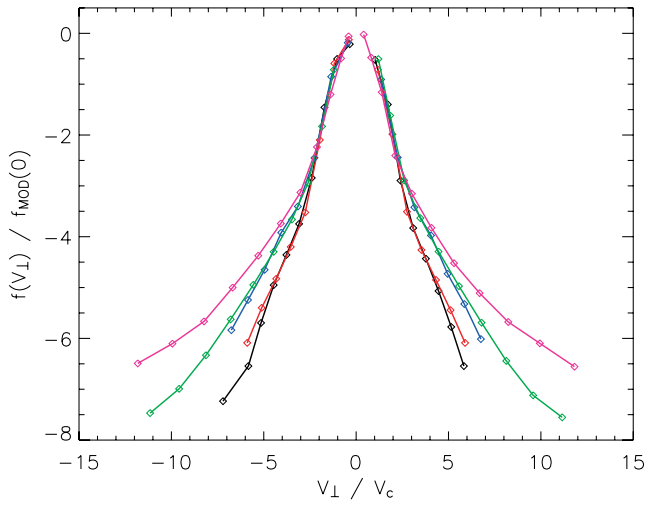

Figure 5. The ratios $f/f_{mod}(0)$ are plotted as a function of $v_\perp/V_c$, for the different radial distances. As one can see, the normalized core component remains unchanged at all radial distances and the relative number of halo electrons, compared to the one of the core, increases with radial distance.

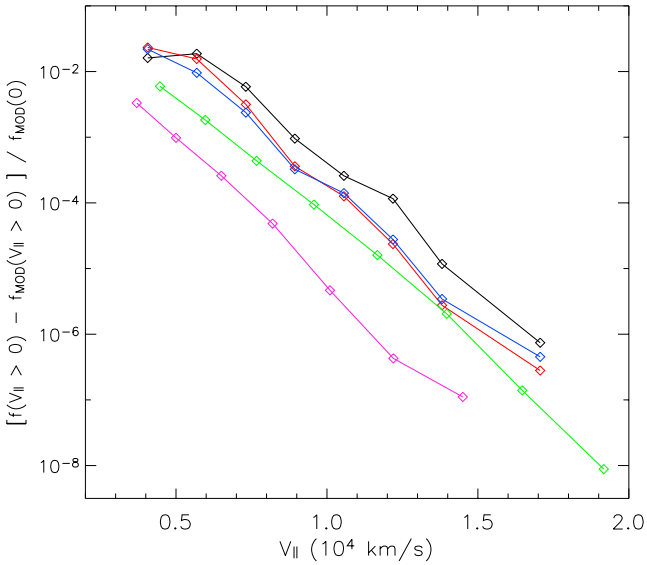

Figure 6. The ratios $[f(v_{\|} > 0) - f_{mod}(v_{\|} > 0)]/f_{mod}(0)$ are plotted as a function of $v_{\|}$, for the different radial distances. This figure illustrates the radial variation of the strahl number density. It can be also noted that the distribution function of the strahl electrons is roughly an exponential function of the particles velocity in the entire radial range from 0.3 to 1.5 AU.

keep only the strahl electrons. This is done by computing $f^* - f_{mod}$, since by definition f_{mod} contains only the core and the halo components. In Figure 6 we therefore plot $[f(v_{\|} > 0) - f_{mod}(v_{\|} > 0)]/f_{mod}(0)$. This figure illustrates the radial variation of the strahl number density. From Figure 6 it can be firstly noted that the distribution function of the strahl electrons is roughly an exponential function of the particle velocity in the entire radial range from 0.3 to 1.5 AU, since all the plotted cuts are roughly linear in the log-linear plot. Secondly, it can be noted that the importance of the strahl electrons decreases with distance.

[23] It is possible to better quantify the findings we presented from Figures 5 and 6. For this purpose, let us compute directly the strahl number density n_s that we define as:

$$n_s = 2\pi \int_0^{\pi} \sin\theta d\theta \int_0^{\infty} (f^* - f_{mod}) v^2 dv.$$

[24] Since we assume that the strahl component is only present on the angular bins 2, 3 and 4, we have actually performed the numerical integration of the above integral only for these three angular bins, for all the speed bins. Practically, we have taken into account only those (v_i, θ_i) integration bins where the quantity $f^* - f_{mod}$ is found to be positive. This condition is met most of the time, with a few exceptions due to the fact that statistical fluctuations of the electron fluxes on a specific (v_i, θ_i) integration bin can be such, that $f^* - f_{mod}$ happens to be negative. Uncertainties on n_s can also be determined by estimating the error on the angular extension of the strahl. This estimate is made because of the incomplete coverage of the unit sphere in Figure 2. The way the computation of the strahl number density is done in our fitting procedure is described in Appendix A.

[25] The results of the computation of the strahl number density is presented in Figure 7. We represent the radial variations of the relative number density, or the fraction of the total density, for the core, halo and strahl components, respectively n_c/n_e, n_h/n_e and n_s/n_e, where $n_e = n_c + n_h + n_s$. The behavior of the fractional densities confirms the previous findings of our analysis. The core relative number density remains roughly constant over the whole radial range, even if a somehow abrupt change occurs for the last radial bin. This latter correspond to the Ulysses radial coverage for which the plasma is so tenuous and the core temperature is so low that the corrections of the photoelectrons and spacecraft charging effects probably start to be critical. The fitting procedure for the VDF corresponding to this radial bin yields therefore larger uncertainties. However we still argue that the core relative number density remains constant within the errors bars. This can be clearly seen in Figure 7 where a straight line, representing a constant value of the core relative number density, can be drawn to pass exactly within the error bars and for all the radial bins.

[26] Concerning now the halo and strahl fractional densities, while they are roughly equal between 0.3 AU and 0.5 AU, representing each about 5 to 9% of the total density, they vary clearly oppositely with increasing radial distance. The halo fractional density increases to reach values of 10 to 30% of the total density at 1.5 AU. Concurrently the strahl number density decreases to values of 1 to 2% of the total density. The results in Figure 7 suggest that during the solar wind transport between 0.3 AU

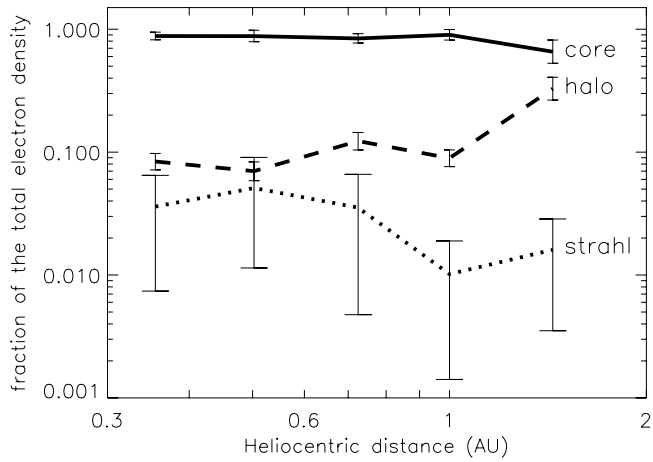

Figure 7. Radial variations of the relative number density, or fractional density, for the core (full line), halo (dashed line), and strahl (dotted line) components, respectively, n_c/n_e, n_h/n_e, and n_s/n_e, where $n_e = n_c + n_h + n_s$. The core relative number density remains roughly constant over the whole radial range. While they are roughly equal between 0.3 and 0.5 AU, the halo and strahl fractional densities vary clearly oppositely with radial distance. These results suggest that during the solar wind transport between 0.3 and 1.5 AU, an important fraction of the strahl electrons may be diffused and transferred to the halo electron population.

and 1.5 AU, an important fraction of the strahl electrons may be diffused and transferred to the halo electron population.

4. Conclusions

[27] In the present article we have studied the radial evolution of the electron velocity distribution functions in the fast solar wind between 0.3 and 1.5 AU. For this purpose, we have combined data measured separately by the Helios, Wind and Ulysses spacecraft. We have computed average distributions over radial bins and normalized them to remove the effects of the solar wind expansion. As a first step, we have modeled only the core and halo components by excluding the angular portion of the distributions where the strahl is present. Then we have removed the core and halo electrons from the observed distributions in order to model the strahl alone. This technique has allowed us to compute the relative number density or fraction of the total density for the core, halo and strahl components. We have observed that, while the core fraction density remains roughly constant with radial distance, the halo and strahl fraction densities vary oppositely with distance. The relative number of halo electrons is increasing while the relative number of strahl electrons is decreasing. Therefore we have provided, for the first time, evidence that the heliospheric electron halo population consist partly of electrons that have been scattered out of the strahl.

[28] Given the low level of collisionality for the strahl electrons, the mechanism that can explain their scattering involves necessarily particle/wave interactions or large-scale field inhomogeneities. For instance whistler heat flux instability, using the linear Vlasov theory has been extensively studied in the solar wind [see *Gary and Li*, 2000, and references therein]. Nevertheless, a comprehensive model that explains the scattering of the strahl electrons is still needed.

[29] Finally, even if it appears from the present study that the halo component of the solar wind electrons may originate from the strahl, a question remains: What is the exact origin of the strahl. Does it exist already in the corona? Does it play a role in the solar wind acceleration mechanisms? Is it a by-product of the acceleration itself and if so, at what radial distance is it formed? The answers to these questions may have to wait a space probe to visit the solar wind acceleration region of the corona.

Appendix A: Fitting Procedure for the Electron Distribution Functions

[30] As described in section 3.1, we use as the best fit to the core + halo part of the observed electron VDFs the sum of a bi-Maxwellian for the core population plus a bi-kappa for the halo, $f_{mod}(v_{\|}, v_{\perp}) = f_c(v_{\|}, v_{\perp}) + f_h(v_{\|}, v_{\perp})$. Fittings of this kind are not easy to carry out. For instance the break-point energy (E_B) between the core and halo component is not determined in a straightforward manner by the minimization of the χ^2 function. Since we wish to model each of the core, halo and strahl components independently of each other, we preselect the data from a visual inspection and applied the following procedure.

[31] First of all, we plot for each of the five radial bins the observed electron fluxes as a function of the electron energy,

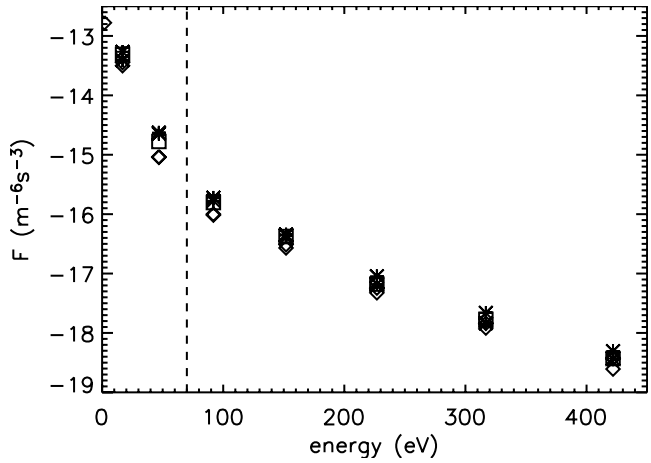

Figure A1. Observed electron fluxes as a function of the electron energy, for the radial bin 3 (0.7–0.75 AU). The diamonds, stars, and squares represent the electron fluxes for, respectively, the angular bins 1 and 5 (the $\perp$ direction), the angular bins 6 and 8, and the angular bin 7 (the $\|$ anti-sunward direction); that is, all the angular bins which do not contain the strahl population. The break-point energy between the core and the halo components, E_B, is indicated by the vertical dashed line. The core component corresponds to all energies lower than E_B, while the halo component correspond to the energies larger than E_B.

for all the angular bins which do not contain the strahl population, that is for all the bins except bins 2, 3 and 4 in Figure 2. The purpose of doing such is that for a Maxwellian distribution, the flux in a log scale is directly proportional to the energy times $-1/k_BT$. Therefore on such a plot E_B should appear as a break on the slopes of the respective core and halo electron fluxes. Figure A1 shows an example of such a plot. In this figure, we display the data for the radial bin 3 (0.7 to 0.75 AU). The diamonds, stars and squares represent the electron fluxes for, respectively, the angular bins 1 and 5 (the $\perp$ direction), the angular bins 6 and 8 and the angular bin 7 (the $\|$ anti-sunward direction). From this plot, E_B appears clearly from a visual examination. It is indicated by the vertical dashed line. The core component correspond to all energies lower than E_B, while the halo component correspond to the energies larger than E_B.

[32] Once we select the observed fluxes corresponding to the core population, we fit them with the bi-Maxwellian model $f_c(v_{\|}, v_{\perp})$ defined in section 3.1, using a classical χ^2 minimization scheme. When doing that, we assume that the contribution of the halo component to the total distribution is negligible. Actually the error we make in neglecting the halo contribution is of the order of f_h/f_c. In the velocity range corresponding to the core electrons this latter quantity is typically of the order of $(n_h/n_c) \times (T_c/T_h)^{3/2}$, that is ranging from roughly 2 to 5%.

[33] Once we have fitted the core population, we remove the obtained $f_c(v_{\|}, v_{\perp})$ model from the observed distributions. We assume that this remaining part of the observed distribution is the halo component. We then fit this remaining part, from E_B to the maximum observed electron energy, with the bi-kappa model $f_h(v_{\|}, v_{\perp})$ defined in section 3.1.

[34] Finally, we remove the obtained $f_{mod}(v_{\|}, v_{\perp}) = f_c(v_{\|}, v_{\perp}) + f_h(v_{\|}, v_{\perp})$ model from the whole observed distribution function and compute, from the remaining part and for the angular bins 1, 2 and 3, the strahl's number density as described in section 3.2.

[35] **Acknowledgments.** Shadia Rifai Habbal thanks C. Vocks and Adolfo F. Vinas for their assistance in evaluating this paper.

References

Bame, S. J., et al. (1992), The Ulysses solar wind plasma experiment, *Astron. Astrophys. Suppl. Ser.*, *92*, 237.

Chiuderi, C., and F. Chiuderi Drago (2004), Effect of suprathermal particles on the quiet Sun radio emission, *Astron. Astrophys.*, *422*, 331–336, doi:10.1051/0004-6361:20035787.

Dorelli, J. C., and J. D. Scudder (2003), Electron heat flow in the solar corona: Implications of non-Maxwellian velocity distributions, the solar gravitational field, and Coulomb collisions, *J. Geophys. Res.*, *108*(A7), 1294, doi:10.1029/2002JA009484.

Esser, R., and R. J. Edgar (2000), Reconciling Spectroscopic electron temperature measurements in the solar corona with in situ charge state observations, *Astrophys. J.*, *532*, L71–L74.

Feldman, W. C., J. R. Asbridge, S. J. Bame, M. D. Montgomery, and S. P. Gary (1975), Solar wind electrons, *J. Geophys. Res.*, *80*, 4181–4196.

Gary, S. P., and H. Li (2000), Whistler heat flux instability at high beta, *Astrophys. J.*, *529*, 1131–1135.

Gosling, J. T., R. M. Skoug, and W. C. Feldman (2001), Solar wind electron halo depletions at 90 pitch angle, *Geophys. Res. Lett.*, *28*, 4155–4158.

Hammond, C. M., W. C. Feldman, D. J. McComas, J. L. Phillips, and R. J. Forsyth (1996), Variation of electron-strahl width in the high-speed solar wind: ULYSSES observations, *Astron. Astrophys.*, *316*, 350–354.

Issautier, K., N. Meyer-Vernet, M. Moncuquet, and S. Hoang (1998), Solar wind radial and latitudinal structure: Electron density and core temperature from ULYSSES thermal noise spectroscopy, *J. Geophys. Res.*, *103*, 1969.

Ko, Y. K., J. Geiss, and G. Locker (1998), On the differential ion velocity in the inner solar corona and the observed solar wind ionic charge states, *J. Geophys. Res.*, *103*, 14,539–14,546.

Landi, S., and F. G. E. Pantellini (2001), On the temperature profile and heat flux in the solar corona: Kinetic simulations, *Astron. Astrophys.*, *372*, 686–701.

Leubner, M. P. (2002), A nonextensive entropy approach to kappa-distributions, *Astrophys. Space Sci.*, *282*, 573–579.

Lie-Svendsen, V. H. Hansteen, and E. Leer (1997), Kinetic electrons in high-speed solar wind streams: Formation of high-energy tails, *J. Geophys. Res.*, *102*, 4701–4718.

Lin, R. P., et al. (1995), A three-dimensional plasma and energetic particle investigation for the Wind spacecraft, *Space. Sci. Rev.*, *71*, 125.

Maksimovic, M., V. Pierrard, and J. Lemaire (1997a), A kinetic model of the solar wind with Kappa distribution functions in the corona, *Astron. Astrophys.*, *324*, 725–734.

Maksimovic, M., V. Pierrard, and P. Riley (1997b), Ulysses electron distributions fitted with Kappa functions, *Geophys. Res. Lett.*, *24*, 1151–1154.

Maksimovic, M., S. P. Gary, and R. M. Skoug (2000), Solar wind electron suprathermal strength and temperature gradients: Ulysses observations, *J. Geophys. Res.*, *105*, 18,337.

Maksimovic, M., V. Pierrard, and J. Lemaire (2001), On the exospheric approach for the solar wind acceleration, *Astrophys. Space Sci.*, *277*, 181–187.

McComas, D. J., S. J. Bame, W. C. Feldman, J. T. Gosling, and J. L. Phillips (1992), Solar wind halo electrons from 1–4 AU, *Geophys. Res. Lett.*, *19*, 1291.

Montgomery, M. D., S. J. Bame, and A. J. Hundhausen (1968), Solar wind electrons: Vela 4 measurements, *J. Geophys. Res.*, *73*, 4999–5003.

Pierrard, V., M. Maksimovic, and J. Lemaire (1999), Electronic velocity distribution functions from the solar wind to the corona, *J. Geophys. Res.*, *104*, 17,021–17,032.

Pierrard, V., M. Maksimovic, and J. Lemaire (2001), Self-consistent model of solar wind electrons, *J. Geophys. Res.*, *106*, 29,305–29,312.

Pilipp, W. G., H. Miggenrieder, M. D. Montgomery, K.-H. Muhlhauser, H. Rosenbauer, and R. Schwenn (1987), Characteristics of electron distribution functions in the solar wind derived from the Helios plasma experiment, *J. Geophys. Res.*, *92*, 1075.

Pinfield, D. J., F. P. Keenan, M. Mathioudakis, K. J. H. Phillips, W. Curdt, and K. Wilhelm (1999), Evidence for non-Maxwellian electron energy distributions in the solar transition region: Si III line ratios from SUMER, *Astrophys. J.*, *527*, 1000–1008.

Rosenbauer, H., et al. (1977), A survey on initial results of the Helios plasma experiment, *J. Geophys.*, *42*, 561.

Salem, C., J.-M. Bosqued, D. E. Larson, A. Mangeney, M. Maksimovic, C. Perche, R. P. Lin, and J.-L. Bougeret (2001), Determination of accurate solar wind electron parameters using particle detectors and radio wave receivers, *J. Geophys. Res.*, *106*, 21,701.

Schwenn, R., H. Rosenbauer, and H. Miggenrieder (1975), Das Plasma-experiment auf Helios (E1), *Raumfahrtforschung*, *19*, 226.

Scime, E. E., J. L. Phillips, and S. J. Bame (1994), Effects of spacecraft potential on three-dimensional electron measurements in the solar wind, *J. Geophys. Res.*, *99*, 14,769.

Shoub, E. C. (1983), Invalidity of local thermodynamic equilibrium for electrons in the solar transition region. I - Fokker-Planck results, *Astrophys. J.*, *266*, 339–369.

Vinas, A. F., H. K. Wong, and A. J. Klimas (2000), Generation of electron suprathermal tails in the upper solar atmosphere: Implications for coronal heating, *Astrophys. J.*, *528*, 509–523.

Vocks, C., and G. Mann (2003), Generation of suprathermal electrons by resonant wave particle interaction in the solar corona and wind, *Astrophys. J.*, *593*, 1134–1145.

Zouganelis, I., M. Maksimovic, N. Meyer-Vernet, H. Lamy, and K. Issautier (2004), A transonic collisionless model of the solar wind, *Astrophys. J.*, *606*, 542–554.

J.-Y. Chaufray, Service d'Aéronomie du CNRS, Route des Gatines, BP 3, F-91371 Verrières Le Buisson, France.

K. Issautier, M. Maksimovic, and I. Zouganelis, LESIA, Observatoire de Paris-Meudon, F-92195 Meudon cedex, France. (milan.maksimovic@obspm.fr)

R. P. Lin and C. Salem, Space Sciences Laboratory, University of California, Berkeley, 7 Gauss Way, 7450, Berkeley, CA 94720-7450, USA.

J. E. Littleton and E. E. Scime, Department of Physics, West Virginia University, P.O. Box 6315, Morgantown, WV 26506, USA.

E. Marsch, Max-Planck-Institut für Sonnensystemforschung, Max-Planck-Strasse 2, D-37191 Katlenburg-Lindau, Germany.

D. J. McComas and H. Elliott, Space Science and Engineering Division, Southwest Research Institute, P.O. Drawer 28510, San Antonio, TX 78228-0510, USA.